THREE DIMENSIONAL PATH FOLLOWING CONTROL FOR A FIXED-WING UAV ON SO(3) WITH INPUT SATURATION

Bo Zhang[1], Wei Li[2], Zhikun Miao[1] & Ying Zhang[3]

[1]Northwestern Polytechnical University
[2]The Second Representative Office of Air Force Armament Department in Luoyang
[3]Beijing System Design Institute of Mechanical-Electrical Engineering

Abstract

This paper addresses the 3D path-following control problem of a fixed-wing UAV on SO(3). To accelerate the convergence to the path and consider the control input saturation and external disturbances, an adaptive control scheme for the 3D path-following problem is proposed. First, an adaptive auxiliary frame is introduced so that the velocity vector of the UAV is nearly perpendicular to the path when the UAV is far from the path and the velocity vector is almost along the tangent of the path when the UAV is close to the path. The adaptive auxiliary frame accelerates the convergence of the path-following control scheme significantly. Based on the adaptive auxiliary frame, the models of the path-following error and attitude error are established. Then a control law for the progression rate of the virtual target and a saturated attitude control law with varying gains are proposed to stabilize the 3D path-following system jointly in the presence of external disturbances. The stability of the closed-loop system and the singularity avoidance is proved via Lyapunov analysis. Finally, numerical simulations are conducted to demonstrate the effectiveness of the proposed scheme.

Keywords: fixed-wing UAVs; 3D path-following; input saturation; SO(3)

1. Introduction

To accomplish specific tasks, UAVs must follow predefined paths, so path-following control is essential to UAVs. Compared with trajectory tracking, path following possesses several advantages [1]: The convergence of path-following controllers is typically smoother than that of trajectory-tracking algorithms; Moreover, path-following algorithms do not impose specific temporal requirements on the vehicle motion; As a result, the speed of the vehicle can be adjusted at will (online, by a human operator, or simply set to a constant value), which becomes a path-independent extra degree of freedom that can be fully used to regulate the path-following controller.

Path-following methods are usually classified into three categories: geometric methods, vector field methods, and control-technique-based methods [3, 4]. The early work of geometric methods can be found in [5, 6, 7, 8], including the pure pursuit method, the carrot-chasing method, the LOS method, and their variants. Geometric methods are designed according to the geometric relation between the velocity of the UAV and the virtual target base on the kinematics of the UAV. Geometric methods are easy to implement but are not accurate enough [9, 1]. The vector field method virtually places a set of vectors around the path in such a way that the vehicle will converge into the path if the vehicle follows the direction of the vectors. The desired course can be generated by those vectors as the inputs of the inner-loop attitude controllers. The vector field method applied to UAVs was reported in [11] for the first time. Pothen and Ratnoo [12] proposed a Lyapunov vector field with a modified circulation term for standoff target tracking. Compared with the conventional vector field, the proposed vector field has a faster settling. In [10], a gradient vector field was optimized so that the gradient vector field guidance can be used for obstacle avoidance with minimal deviations from an original path. The vector field method is suitable for following a straight-line path and a circular path. For a general path, it is hard to construct a corresponding vector field. The path-following method based on control theory is accurate enough and can be applied to any paths. A path-following control scheme based on the high-order sliding mode control theory was proposed in [13] with a nonlinear sliding surface used and saturation of the guidance commands considered. Hamada et al. [14]

applied the nonlinear receding horizon optimization technique to the planar path following of a small UAV. In [15], Chen t al proposed a new path-following guidance scheme by combining the virtual target concept and a missile terminal guidance law, which possesses high accuracy and fast convergence. By using geometric concepts, Jain et al. [16] developed a control scheme to follow a geometric path specified with respect to a reference frame moving in three dimensions using geometric concepts, wherein the attitude control problem is formulated on the Special Orthogonal group SO(3).

The path-following control problem of UAVs has been studied extensively, but most of them just follow a planar path and do not consider the minimal velocity requirement of fixed-wing UAVs. Though Cichella et al. [17] addressed the 3D path-following control scheme on SO(3) for a fixed-wing UAV, the physical limit of the UAV's angular rate and external disturbances are not considered and the convergence rate to the path is not fast enough. To cope with the issues, an adaptive path-following control scheme with saturation considered is developed on SO(3) in this paper. First, an adaptive auxiliary frame is introduced to accelerate the convergence of the path-following control scheme, based on which the models of path-following error and attitude error are established. Then a control law for the progression rate of the virtual target and a saturated attitude control law with varying gains are proposed to stabilize the 3D path-following system in the presence of external disturbances.

This paper is organized as follows. In Section 2, the 3D path-following problem is formulated on SO(3). In Section 3, the path-following control scheme is developed. Section 4 gives the simulation results to validate the effectiveness of the proposed algorithm. Section 5 concludes this paper.

2. Problem Formulation

Before proceeding to the formulation of the 3D path-following problem, some useful coordinate frames are introduced firstly. The inertial frame is a right-handed frame fixed on the ground and denoted by $\mathcal{F}_I$. The axes of $\mathcal{F}_I$ are determined by a triple $\{x_I, y_I, z_I\}$, where x_I, y_I, and z_I are orthogonal unit vectors. To described the attitude motion of the UAV, a velocity coordinate frame $\mathcal{F}_W$ is introduced. The origin of $\mathcal{F}_W$ is at the mass center of the UAV, and its x-axis is aligned with the velocity vector of the UAV. The z-axis of $\mathcal{F}_W$ is perpendicular to the x-axis and points upward in the symmetric plane of the UAV. The y-axis completes the right-handed frame. To follow the path, a virtual target moving along the desired path is introduced and denoted by P. Let $\boldsymbol{p}_{PI}(s)$ be the position vector of the virtual target relative to $\mathcal{F}_I$, where s is a variable that defines the instant position of the virtual target on the path. A parallel transport frame $\mathcal{F}_P$ is right-handed and attached to the point P, which is defined by a triple $\{\boldsymbol{t}(s), \boldsymbol{n}_1(s), \boldsymbol{n}_2(s)\}$. The unit vector $\boldsymbol{t}$ defines the tangent direction to the path at the point P, while $\boldsymbol{n}_1$ and $\boldsymbol{n}_2$ are orthogonal and define the plane perpendicular to $\boldsymbol{t}$. The triple satisfies the following equation [1]:

$$\begin{bmatrix} \frac{\mathrm{d}\boldsymbol{t}}{\mathrm{d}s}(s) \\ \frac{\mathrm{d}\boldsymbol{n}_1}{\mathrm{d}s}(s) \\ \frac{\mathrm{d}\boldsymbol{n}_2}{\mathrm{d}s}(s) \end{bmatrix} = \begin{bmatrix} 0 & k_1(s) & k_2(s) \\ -k_1(s) & 0 & 0 \\ -k_2(s) & 0 & 0 \end{bmatrix} \begin{bmatrix} \boldsymbol{t}(s) \\ \boldsymbol{n}_1(s) \\ \boldsymbol{n}_1(s) \end{bmatrix} \tag{1}$$

where $k_1(s)$ and $k_2(s)$ are related to the polar coordinate of the curvature $\kappa(s)$ and torsion $\tau(s)$ as

$$\kappa(s) = \sqrt{k_1^2(s) + k_2^2(s)} \tag{2}$$

$$\tau(s) = -\frac{\mathrm{d}}{\mathrm{d}s}\left[\arctan\left(\frac{k_2(s)}{k_1(s)}\right)\right] \tag{3}$$

Then, the dynamics of $\mathcal{F}_P$ can be described by

$$\frac{\mathrm{d}\boldsymbol{t}}{\mathrm{d}t} = [k_1(s)\boldsymbol{n}_1 + k_2(s)\boldsymbol{n}_2]\dot{s} \tag{4}$$

$$\frac{\mathrm{d}\boldsymbol{n}_1}{\mathrm{d}t} = -k_1(s)\boldsymbol{t}\dot{s} \tag{5}$$

$$\frac{\mathrm{d}\boldsymbol{n}_2}{\mathrm{d}t} = -k_2(s)\boldsymbol{t}\dot{s} \tag{6}$$

The relations between the frames are illustrated in Fig. 1.

The angular velocity of $\mathcal{F}_P$ with respect to $\mathcal{F}_I$ is expressed in $\mathcal{F}_P$ as

$$\omega_{PI}^{P} = [0, -k_2(s)\dot{s}, k_1(s)\dot{s}]^{\mathsf{T}} \tag{7}$$
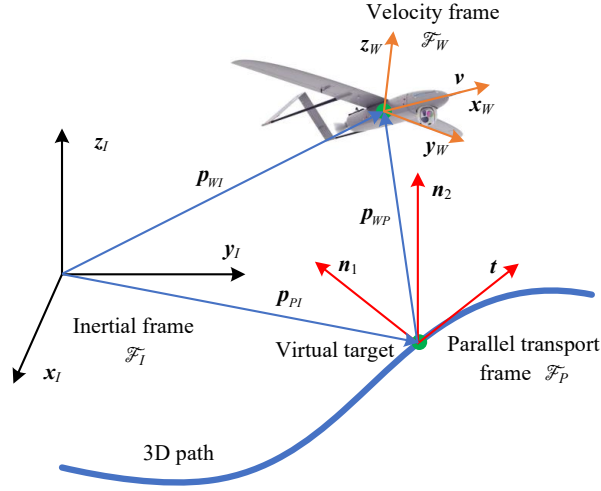
Figure 1 – Illustration of the path-following geometry.

The position of the UAV's mass center can be represented by the position vector of $\mathcal{F}_W$ relative to $\mathcal{F}_P$, which is resolved in $\mathcal{F}_P$ as

$$\boldsymbol{p}_{WP}^P = [x_P, \ y_P, \ z_P]^\mathsf{T} \tag{8}$$

Then the position of the UAV's mass center with respect to $\mathcal{F}_I$ is obtained by

$$\boldsymbol{p}_{WI} = \boldsymbol{p}_{PI} + \boldsymbol{p}_{WP} \tag{9}$$

The time derivative of $\boldsymbol{p}_{WI}$ taken in $\mathcal{F}_I$ is given by

$$^I\dot{\boldsymbol{p}}_{WI} = \dot{s}\boldsymbol{t} + \boldsymbol{\omega}_{PI} \times \boldsymbol{p}_{WP} + {}^P\dot{\boldsymbol{p}}_{WP} \tag{10}$$

where $\dot{s}$ is the progression rate of the virtual target, $\boldsymbol{\omega}_{PI}$ is the velocity vector of $\mathcal{F}_P$ with respect to $\mathcal{F}_I$, and $^P\dot{\boldsymbol{p}}_{WP}$ represents the time derivative of $\boldsymbol{p}_{WP}$ taken in $\mathcal{F}_P$. Since we also have that

$$^I\dot{\boldsymbol{p}}_{WI} = v\boldsymbol{x}_W \tag{11}$$

where v denotes the magnitude of the UAV's velocity vector, the dynamics of the position error between the UAV and $\mathcal{F}_P$ is

$$^P\dot{\boldsymbol{p}}_{WP} = -\dot{s}\boldsymbol{t} - \boldsymbol{\omega}_{PI} \times \boldsymbol{p}_{WP} + v\boldsymbol{x}_W \tag{12}$$

Eq. (12) resolved in $\mathcal{F}_P$ is given by

$$\begin{bmatrix} \dot{x}_P \\ \dot{y}_P \\ \dot{z}_P \end{bmatrix} = - \begin{bmatrix} \dot{s} \\ 0 \\ 0 \end{bmatrix} - \left(\begin{bmatrix} 0 \\ -k_2(s)\dot{s} \\ k_1(s)\dot{s} \end{bmatrix} \times \begin{bmatrix} x_P \\ y_P \\ z_P \end{bmatrix} \right) + \boldsymbol{R}_W^F \begin{bmatrix} v \\ 0 \\ 0 \end{bmatrix} \tag{13}$$

When the UAV is far from the path, it should approach the path as fast as possible. Hence, the velocity should be almost perpendicular to the path. As the UAV is in the vicinity of the path, the UAV is preferred to fly along the tangent of the path. Though this goal was achieved roughly in [17] by using an auxiliary frame, the convergent performance can be further improved by introducing an adaptive term into the definition of the frame. The adaptive auxiliary frame is defined by an unit vector triple $\{\boldsymbol{x}_D, \boldsymbol{y}_D, \boldsymbol{z}_D\}$, which is given by

$$\boldsymbol{x}_D = \frac{h\boldsymbol{t} - \boldsymbol{p}_\times}{\sqrt{h^2 + \|\boldsymbol{p}_\times\|_2}} \tag{14}$$

$$\boldsymbol{y}_D = \frac{y_P\boldsymbol{t} + h\boldsymbol{n}_1}{\sqrt{h^2 + y_P^2}} \tag{15}$$

$$\boldsymbol{z}_D = \boldsymbol{x}_D \times \boldsymbol{y}_D \tag{16}$$

3

where $h > 0$ is the parameter that needs to be designed to enhance the path-following performance, and $\boldsymbol{p}_\times = y_P \boldsymbol{n}_1 + z_P \boldsymbol{n}_2$ is the cross tracking error vector of the UAV with respect to the path. To achieve the goal of the path-following, h should be large when the UAV is far from the path and small when it is close to the path. The orthonormal basis of $\mathcal{F}_D$ can be used to construct the rotation matrix from $\mathcal{F}_D$ to $\mathcal{F}_I$ as

$$\boldsymbol{R}_D^I = \left[\boldsymbol{x}_D^I, \, \boldsymbol{y}_D^I, \, \boldsymbol{z}_D^I \right] = \boldsymbol{R}_P^I \left[\boldsymbol{x}_D^P, \, \boldsymbol{y}_D^P, \, \boldsymbol{z}_D^P \right] \tag{17}$$

where $\boldsymbol{x}_D^I$, $\boldsymbol{y}_D^I$, and $\boldsymbol{z}_D^I$ are the coordinates of the vectors $\boldsymbol{x}_D$, $\boldsymbol{y}_D$, and $\boldsymbol{z}_D$ expressed in $\mathcal{F}_I$, respectively. The superscript P indicates the vectors are resolved in $\mathcal{F}_P$. Similarly, the rotation matrix from $\mathcal{F}_P$ to $\mathcal{F}_I$ is given by

$$\boldsymbol{R}_P^I = \left[\boldsymbol{t}^I, \, \boldsymbol{n}_1^I, \, \boldsymbol{n}_2^I \right] = \boldsymbol{R}_P^I \left[\boldsymbol{t}^P, \, \boldsymbol{n}_1^P, \, \boldsymbol{n}_2^P \right] \tag{18}$$

Hence, the rotation matrix from $\mathcal{F}_D$ to $\mathcal{F}_P$ can be obtained by

$$\boldsymbol{R}_D^P = \left(\boldsymbol{R}_F^I \right)^\top \boldsymbol{R}_D^I = \begin{bmatrix} \dfrac{h}{\sqrt{h^2 + y_P^2 + z_P^2}} & \dfrac{y_P}{\sqrt{h^2 + y_P^2}} & \dfrac{z_P h}{\sqrt{(h^2 + y_P^2 + z_P^2)(h^2 + y_P^2)}} \\ \dfrac{-y_P}{\sqrt{h^2 + y_P^2 + z_P^2}} & \dfrac{h}{\sqrt{h^2 + y_P^2}} & \dfrac{-y_P z_P}{\sqrt{(h^2 + y_P^2 + z_P^2)(h^2 + y_P^2)}} \\ \dfrac{-z_P}{\sqrt{h^2 + y_P^2 + z_P^2}} & 0 & \dfrac{\sqrt{h^2 + y_P^2}}{\sqrt{h^2 + y_P^2 + z_P^2}} \end{bmatrix} \tag{19}$$

The rotation matrix from $\mathcal{F}_W$ to $\mathcal{F}_D$ is

$$\boldsymbol{R}_W^D = \left(\boldsymbol{R}_D^P \right)^\top \boldsymbol{R}_W^P \tag{20}$$

where $\boldsymbol{R}_W^P$ is determined by

$$\dot{\boldsymbol{R}}_W^P = \boldsymbol{R}_W^P \left(\omega_{WP}^W \right)^\wedge \tag{21}$$

where $(\bullet)^\wedge : \mathbb{R}^3 \to so(3)$ denotes the hat map [1], and ω_{WP}^W is the angular velocity of $\mathcal{F}_W$ with respect to $\mathcal{F}_P$ expressed in $\mathcal{F}_W$. One of the control objectives is to steer the UAV's velocity to coincide with the x-axis of $\mathcal{F}_D$, so the attitude error on SO(3) is defined by

$$\Psi \left(\tilde{\boldsymbol{R}} \right) = \frac{1}{2} \mathrm{tr} \left[\left(\boldsymbol{I}_3 - \boldsymbol{\Pi}_R^\top \boldsymbol{\Pi}_R \right) \left(\boldsymbol{I}_3 - \tilde{\boldsymbol{R}} \right) \right] \tag{22}$$

where $\tilde{\boldsymbol{R}} = \boldsymbol{R}_W^D$, and $\mathrm{tr}(\bullet)$ represents the trace of a matrix. The matrix $\boldsymbol{\Pi}$ is given by

$$\boldsymbol{\Pi}_R = \begin{bmatrix} 0 & 1 & 0 \\ 0 & 0 & 1 \end{bmatrix} \tag{23}$$

Thus, Eq. (22) is equivalent to

$$\Psi \left(\tilde{\boldsymbol{R}} \right) = \frac{1}{2} \left(1 - \tilde{R}_{11} \right) \tag{24}$$

where $\tilde{R}_{11}$ represents the (1,1) entry of $\tilde{\boldsymbol{R}}$. It should be noted that $\tilde{R}_{11} = 1$ implies that the UAV's velocity vector is aligned with the x-axis of $\mathcal{F}_D$ (i.e. unit vector $\boldsymbol{x}_D$), which defines the desired attitude of the vehicle. The relative attitude kinematics between $\mathcal{F}_W$ and $\mathcal{F}_D$ is described by

$$\dot{\tilde{\boldsymbol{R}}} = \tilde{\boldsymbol{R}} \left(\omega_{WD}^W \right)^\wedge \tag{25}$$

where ω_{WD}^W denotes the angular velocity of $\mathcal{F}_W$ with respect to $\mathcal{F}_D$ resolved in $\mathcal{F}_W$. Substituting Eq. (25) into the time derivative of Eq. (22), one obtains the dynamics of the attitude error as

$$\dot{\Psi} \left(\tilde{\boldsymbol{R}} \right) = -\frac{1}{2} \mathrm{tr} \left[\left(\boldsymbol{I}_3 - \boldsymbol{\Pi}_R^\top \boldsymbol{\Pi}_R \right) \tilde{\boldsymbol{R}} \left(\omega_{WD}^W \right)^\wedge \right] \tag{26}$$

After some algebraic operations, the following equation is obtained:

$$\dot{\Psi} \left(\tilde{\boldsymbol{R}} \right) = \left\{ \frac{1}{2} \boldsymbol{\Pi}_R \left[\left(\boldsymbol{I}_3 - \boldsymbol{\Pi}_R^\top \boldsymbol{\Pi}_R \right) \tilde{\boldsymbol{R}} - \tilde{\boldsymbol{R}}^\top \left(\boldsymbol{I}_3 - \boldsymbol{\Pi}_R^\top \boldsymbol{\Pi}_R \right) \right]^\vee \right\}^\top \boldsymbol{\Pi}_R \omega_{WD}^W \tag{27}$$

4

where $(\bullet)^\vee : so(3) \rightarrow \mathbb{R}^3$ denotes the vee map [1]. Define the attitude error of the UAV with respect to $\mathcal{F}_W$ as

$$e_{\tilde{R}} = \frac{1}{2}\boldsymbol{\Pi}_R \left[\left(I_3 - \boldsymbol{\Pi}_R^\top \boldsymbol{\Pi}_R \right) \tilde{R} - \tilde{R}^\top \left(I_3 - \boldsymbol{\Pi}_R^\top \boldsymbol{\Pi}_R \right) \right]^\vee \tag{28}$$

Then, Eq. (27) is simplified to

$$\dot{\Psi}\left(\tilde{R}\right) = e_{\tilde{R}} \cdot \left(\boldsymbol{\Pi}_R \omega_{WD}^W \right) \tag{29}$$

According to the relations between the frames, ω_{WD}^W can be written as

$$\omega_{WD}^W = \omega_{WI}^W - \tilde{R}^\top \left(R_P^D \omega_{PI}^P + \omega_{DP}^D \right) \tag{30}$$

where ω_{WI}^W is the angular velocity of $\mathcal{F}_W$ with respect to $\mathcal{F}_I$ expressed in $\mathcal{F}_W$, ω_{PI}^P is the angular velocity of $\mathcal{F}_P$ with respect to $\mathcal{F}_I$ expressed in $\mathcal{F}_P$, and ω_{DP}^D is the angular velocity of $\mathcal{F}_D$ with respect to $\mathcal{F}_P$ expressed in $\mathcal{F}_D$. Substituting Eq. (30) into Eq. (29) yields

$$\dot{\Psi}\left(\tilde{R}\right) = e_{\tilde{R}} \cdot \left[\boldsymbol{\Pi}_R \omega_{WI}^W - \boldsymbol{\Pi}_R \tilde{R}^\top \left(R_P^D \omega_{PI}^P + \omega_{DP}^D \right) \right] \tag{31}$$

Recalling the definition of $\boldsymbol{\Pi}_R$, one has $\boldsymbol{\Pi}_R \omega_{WI}^W = [q,\ r]^\top$, where q and r are the y-component and z-component of ω_{WI}^W, respectively.

Finally, considering the external disturbances exerted on the UAV, the dynamics of the path-following errors are described by

$$^P\dot{p}_{WP} = -\dot{s}t - \omega_{PI} \times p_{WP} + vx_W + d_1 \tag{32}$$

$$\dot{\Psi}\left(\tilde{R}\right) = e_{\tilde{R}} \cdot \left[u - \boldsymbol{\Pi}_R \tilde{R}^\top \left(R_P^D \omega_{PI}^P + \omega_{DP}^D \right) + d_2 \right] \tag{33}$$

where $u = [q,\ r]^\top$; $d_1 \in \mathbb{R}^3$ and $d_2 \in \mathbb{R}^2$ are disturbances, which are bounded by $\|d_1\|_2 \leq d_{1\max}$ and $\|d_2\|_2 \leq d_{2\max}$. q and r are taken as the inputs of the path-following control scheme, while the rate of progression $\dot{s}$ of the point P along the path becomes an extra variable that can be manipulated at will.

3. Path Following Controller Design

To enhance the convergent rate, and meanwhile, properly damp the path-following control scheme, an adaptive design for the parameter of the auxiliary frame is proposed. Then, on the basis of the path-following error model, a path-following control scheme considering input saturation is developed in the presence of external disturbances.

3.1 Adaptive Auxiliary Frame

When the UAV is far away from the path in the initial phase of the path-following problem, the desired velocity vector should be almost opposite to $p_\times$ to reduce the cross tracking error as fast as possible. However, when the UAV reaches the neighborhood of the path, the UAV may overshoot the path and fly back-and-forth due to the lack of damping if the velocity vector is still opposite to $p_\times$. To solve this problem, we propose an adaptive auxiliary frame by designing h in Eqs. (14) and (15) as follows:

$$h = (h_0 + 2h_1) - h_1 \left[1 + \tanh\left(\delta\|p_\times\|_2 \right) \right] \tag{34}$$

where $h_0, h_1, \delta > 0$ are constant. Obviously,

$$\lim_{\|p_\times\|_2 \to \infty} h = h_0 \tag{35}$$

$$\lim_{\|p_\times\|_2 \to 0} h = h_0 + h_1 \tag{36}$$

According to Eq. (14), a large h implies that x_D is dominated by t and a small h indicates that x_D is nearly opposite to the cross tracking error $p_\times$. If the velocity of the UAV is commanded to coincide with x_D, the UAV will approach the path rapidly with the help of an small h and then fly along the path smoothly by virtue of a large h.

3.2 Path Following Control with Input Saturation

To facilitate the analysis of the control scheme, the following lemma is introduced.

Lemma 1 [2]: For any $a > 0$ and all real scalar x, the following inequality holds

$$x\tanh\left(\frac{x}{a}\right) \geq |x| - a\tanh\left(\frac{|x|}{a}\right) \tag{37}$$

In Eqs. (32) and (33), $\dot{s}$ and $\boldsymbol{u}$ are taken as the control inputs of the path-following model. The progression rate of the virtual target is not implemented by any physical device, so it can be used to assist in stabilizing the path-following control scheme. The control law for the attitude subsystem is proposed as

$$\boldsymbol{u} = -u_m \tanh\left(\frac{\boldsymbol{e}_{\tilde{R}}}{\alpha k^2}\right) \tag{38}$$

where $\alpha > 1$ is constant, and k is given by

$$\dot{k} = -\frac{\beta}{k}\left\{ u_m \alpha k^2 \left[\tanh\left(\frac{|e_1|}{\alpha k^2}\right) + \tanh\left(\frac{|e_2|}{\alpha k^2}\right)\right] + \boldsymbol{e}_{\tilde{R}}^{\mathsf{T}} \boldsymbol{\Pi}_R \tilde{\boldsymbol{R}}^{\mathsf{T}} \omega \tanh\left(\frac{\boldsymbol{e}_{\tilde{R}}^{\mathsf{T}} \boldsymbol{\Pi}_R \tilde{\boldsymbol{R}}^{\mathsf{T}} \omega}{\alpha k^2}\right)\right.$$
$$\left. + \alpha k^2 \tanh\left(\frac{|\boldsymbol{e}_{\tilde{R}}^{\mathsf{T}} \boldsymbol{\Pi}_R \tilde{\boldsymbol{R}}^{\mathsf{T}} \omega|}{\alpha k^2}\right) + \left[\frac{cv}{\varepsilon}(\varepsilon + 1) + cd_{1\max}\right] \|\boldsymbol{p}_{WP}\|_2 \right\} \tag{39}$$

where $\beta > 0$ is constant, and $\varepsilon = \boldsymbol{x}_W^{\mathsf{T}}(\boldsymbol{x}_D + \alpha\boldsymbol{x}_W) = \alpha + \boldsymbol{x}_W^{\mathsf{T}}\boldsymbol{x}_D > 0$; e_1 and e_2 are the first and the second entries of $\boldsymbol{e}_R$, respectively. Then, $\dot{s}$ is designed as

$$\dot{s} = (v\boldsymbol{x}_W + k_s \boldsymbol{p}_{WP}) \cdot \boldsymbol{t} \tag{40}$$

where k_s is given by

$$k_s = \frac{v}{\varepsilon} \frac{1}{\sqrt{h^2 + \|\boldsymbol{p}_\times\|_2^2}} > 0 \tag{41}$$

Theorem 1: Consider the 3D path-following error model of a fixed-wing UAV composed of Eqs. (32) and (33). With the application of the adaptive auxiliary frame $\mathcal{F}_D$, the proposed control law in Eqs. (38) and (40) stabilizes the path-following error system asymptotically in the presence of input saturation and external disturbances. Meanwhile, the parameter k is prevented from being 0 to avoid singularity of the control law.

Proof: Consider the following Lyapunov function candidate

$$V = \Psi + \frac{c}{2}\boldsymbol{p}_{WP} \cdot \boldsymbol{p}_{WP} + \frac{1}{2\beta}k^2 \tag{42}$$

The time derivative of V is

$$\dot{V} = \dot{\Psi} + c\boldsymbol{p}_{WP} \cdot \dot{\boldsymbol{p}}_{WP} + \frac{1}{\beta}k\dot{k}$$
$$= \boldsymbol{e}_R \cdot \left[\boldsymbol{u} - \boldsymbol{\Pi}_R \tilde{\boldsymbol{R}}^{\mathsf{T}}\omega + \boldsymbol{d}_2\right] + c\boldsymbol{p}_{WP} \cdot (-\dot{s}\boldsymbol{t} - \omega_{PI} \times \boldsymbol{p}_{WP} + v\boldsymbol{x}_W + \boldsymbol{d}_1) + \frac{1}{\beta}k\dot{k} \tag{43}$$

where $\omega = \boldsymbol{\Pi}_R \tilde{\boldsymbol{R}}^{\mathsf{T}}\left(\boldsymbol{R}_P^D \omega_{PI}^P + \omega_{DP}^D\right)$. Substituting Eqs. (40) and (38) into (43) yields

$$\dot{V} = -u_m \boldsymbol{e}_{\tilde{R}} \cdot \tanh\left(\frac{\boldsymbol{e}_{\tilde{R}}}{\alpha k^2}\right) - \boldsymbol{e}_{\tilde{R}} \cdot \boldsymbol{\Pi}_R \boldsymbol{R}^{\mathsf{T}}\omega + \boldsymbol{e}_{\tilde{R}} \cdot \boldsymbol{d}_2 - c\boldsymbol{p}_{WP} \cdot [(v\boldsymbol{x}_W + k_s\boldsymbol{p}_{WP}) \cdot \boldsymbol{t}]\boldsymbol{t} + c\boldsymbol{p}_{WP} \cdot v\boldsymbol{x}_W + c\boldsymbol{p}_{WP} \cdot \boldsymbol{d}_1$$
$$+ \frac{1}{\beta}k\dot{k} \tag{44}$$

For the forth term of the right-handed part, we have

$$\boldsymbol{p}_{WP} \cdot [(v\boldsymbol{x}_W + k_s\boldsymbol{p}_{WP}) \cdot \boldsymbol{t}]\boldsymbol{t} = k_s(\boldsymbol{p}_{WP} \cdot \boldsymbol{t})^2 + v\boldsymbol{p}_{WP} \cdot [(\boldsymbol{x}_W \cdot \boldsymbol{t})\boldsymbol{t}] \tag{45}$$

Thus, $\dot{V}$ becomes

$$\dot{V} = -u_m \boldsymbol{e}_{\tilde{R}} \cdot \tanh\left(\frac{\boldsymbol{e}_{\tilde{R}}}{\alpha k^2}\right) - \boldsymbol{e}_{\tilde{R}} \cdot \boldsymbol{\Pi}_R \tilde{\boldsymbol{R}}^{\mathsf{T}}\omega + \boldsymbol{e}_{\tilde{R}} \cdot \boldsymbol{d}_2 - ck_s x_P^2 + cv\boldsymbol{p}_{WP} \cdot [\boldsymbol{x}_W - (\boldsymbol{x}_W \cdot \boldsymbol{t})\boldsymbol{t}] + c\boldsymbol{p}_{WP} \cdot \boldsymbol{d}_1 + \frac{1}{\beta}k\dot{k} \tag{46}$$

6

where x_P is the first element of $\boldsymbol{p}_{WP}^P$. To further reduce Eq. (46), we have to resort to

$$
\begin{aligned}
\boldsymbol{p}_{WP} \cdot [\boldsymbol{x}_W - (\boldsymbol{x}_W \cdot \boldsymbol{t})\boldsymbol{t}] &= (x_P \boldsymbol{t} + \boldsymbol{p}_\times) \cdot [\boldsymbol{x}_W - (\boldsymbol{x}_W \cdot \boldsymbol{t})\boldsymbol{t}] \\
&= x_P \boldsymbol{t} \cdot \boldsymbol{x}_W - x_P (\boldsymbol{x}_W \cdot \boldsymbol{t}) + \boldsymbol{p}_\times^\mathsf{T} \boldsymbol{x}_W \\
&= \boldsymbol{p}_\times^\mathsf{T} \boldsymbol{x}_W \\
&= \boldsymbol{p}_\times^\mathsf{T} \boldsymbol{x}_W + \frac{\boldsymbol{p}_\times^\mathsf{T} (\boldsymbol{x}_D + \alpha \boldsymbol{x}_W)}{\boldsymbol{x}_W^\mathsf{T} (\boldsymbol{x}_D + \alpha \boldsymbol{x}_W)} - \frac{\boldsymbol{p}_\times^\mathsf{T} (\boldsymbol{x}_D + \alpha \boldsymbol{x}_W)}{\boldsymbol{x}_W^\mathsf{T} (\boldsymbol{x}_D + \alpha \boldsymbol{x}_W)} \\
&= \frac{1}{\varepsilon} \left\{ \boldsymbol{p}_\times^\mathsf{T} (\boldsymbol{x}_D + \alpha \boldsymbol{x}_W) + \boldsymbol{p}_\times^\mathsf{T} \left\{ \boldsymbol{x}_W \left[\boldsymbol{x}_W^\mathsf{T} (\boldsymbol{x}_D + \alpha \boldsymbol{x}_W) \right] - (\boldsymbol{x}_D + \alpha \boldsymbol{x}_W) \right\} \right\}
\end{aligned}
\tag{47}
$$

In addition, the following equalities hold:

$$
\boldsymbol{p}_\times^\mathsf{T} (\boldsymbol{x}_D + \alpha \boldsymbol{x}_W) = \boldsymbol{p}_\times^\mathsf{T} \left(\frac{h\boldsymbol{t} - \boldsymbol{p}_\times}{\sqrt{h^2 + \|\boldsymbol{p}_\times\|_2^2}} + \alpha \boldsymbol{x}_W \right) = -\frac{\|\boldsymbol{p}_\times\|_2^2}{\sqrt{h^2 + \|\boldsymbol{p}_\times\|_2^2}} + \alpha \boldsymbol{p}_\times^\mathsf{T} \boldsymbol{x}_W
\tag{48}
$$

$$
\boldsymbol{p}_\times^\mathsf{T} \left\{ \boldsymbol{x}_W \left[\boldsymbol{x}_W^\mathsf{T} (\boldsymbol{x}_D + \alpha \boldsymbol{x}_W) \right] - (\boldsymbol{x}_D + \alpha \boldsymbol{x}_W) \right\} = \boldsymbol{p}_\times^\mathsf{T} \left[\boldsymbol{x}_W (\boldsymbol{x}_W^\mathsf{T} \boldsymbol{x}_D) - \boldsymbol{x}_D \right]
\tag{49}
$$

Hence, we have

$$
\begin{aligned}
\dot{V} ={}& -u_m \boldsymbol{e}_{\tilde{R}} \cdot \tanh\left(\frac{\boldsymbol{e}_{\tilde{R}}}{\alpha k^2} \right) - \boldsymbol{e}_{\tilde{R}} \cdot \boldsymbol{\Pi}_R \tilde{R}^\mathsf{T} \boldsymbol{\omega} + \boldsymbol{e}_{\tilde{R}} \cdot \boldsymbol{d}_2 - c k_s x_P^2 - \frac{cv \|\boldsymbol{p}_\times\|_2^2}{\varepsilon \sqrt{h^2 + \|\boldsymbol{p}_\times\|_2^2}} \\
&+ \frac{cv\alpha}{\varepsilon} \boldsymbol{p}_\times^\mathsf{T} \boldsymbol{x}_W + \frac{cv}{\varepsilon} \boldsymbol{p}_\times^\mathsf{T} \left[\boldsymbol{x}_W (\boldsymbol{x}_W^\mathsf{T} \boldsymbol{x}_D) - \boldsymbol{x}_D \right] + c \boldsymbol{p}_{WP} \cdot \boldsymbol{d}_1 + \frac{1}{\beta} k \dot{k} \\
\leq{}& -u_m \boldsymbol{e}_{\tilde{R}} \cdot \tanh\left(\frac{\boldsymbol{e}_{\tilde{R}}}{\alpha k^2} \right) - \boldsymbol{e}_{\tilde{R}} \cdot \boldsymbol{\Pi}_R \tilde{R}^\mathsf{T} \boldsymbol{\omega} + d_{2\max} \|\boldsymbol{e}_{\tilde{R}}\|_2 - c k_s x_P^2 - \frac{cv}{\varepsilon} \frac{\|\boldsymbol{p}_\times\|_2^2}{\sqrt{h^2 + \|\boldsymbol{p}_\times\|_2^2}} \\
&+ \frac{cv\alpha}{\varepsilon} (\varepsilon + 1) \|\boldsymbol{p}_\times\|_2 + c d_{1\max} \|\boldsymbol{p}_{WP}\|_2 + \frac{1}{\beta} k \dot{k}
\end{aligned}
\tag{50}
$$

In the derivation of Eq. (50), the following inequality is used:

$$
\begin{aligned}
\frac{cv}{\varepsilon} \left\{ \alpha \boldsymbol{p}_\times^\mathsf{T} \boldsymbol{x}_W + \boldsymbol{p}_\times^\mathsf{T} \left[\boldsymbol{x}_W (\boldsymbol{x}_W^\mathsf{T} \boldsymbol{x}_D) - \boldsymbol{x}_D \right] \right\} &= \frac{cv}{\varepsilon} \boldsymbol{p}_\times^\mathsf{T} (\varepsilon \boldsymbol{x}_W - \boldsymbol{x}_D) \leq \frac{cv}{\varepsilon} \|\boldsymbol{p}_\times\|_2 \|\varepsilon \boldsymbol{x}_W - \boldsymbol{x}_D\|_2 \\
&\leq \frac{cv}{\varepsilon} \|\boldsymbol{p}_\times\|_2 (\|\varepsilon \boldsymbol{x}_W\|_2 + \|\boldsymbol{x}_D\|_2) \leq \frac{cv}{\varepsilon} (\varepsilon + 1) \|\boldsymbol{p}_\times\|_2
\end{aligned}
\tag{51}
$$

Substituting Eq. (39) into Eq. (50) and invoking Lemma 1, one has

$$
\begin{aligned}
\dot{V} &\leq -(u_m - d_{2\max}) \|\boldsymbol{e}_{\tilde{R}}\|_1 - c k_s x_P^2 - \frac{cv}{\varepsilon} \frac{\|\boldsymbol{p}_\times\|_2^2}{\sqrt{h^2 + \|\boldsymbol{p}_\times\|_2^2}} \\
&= -(u_m - d_{2\max}) \|\boldsymbol{e}_{\tilde{R}}\|_1 - c k_s \|\boldsymbol{p}_{WP}\|_2^2
\end{aligned}
\tag{52}
$$

where $u_m > d_{2\max}$ because the control input must dominate the dynamic system, or the system is not controllable. Hence, we have $\boldsymbol{e}_{\tilde{R}} \in \mathcal{L}_\infty$, $\boldsymbol{p}_{WP} \in \mathcal{L}_\infty$, and $k \in \mathcal{L}_\infty$. Provided that $\boldsymbol{p}_{WP}$ is bounded by $\|\boldsymbol{p}_{WP}\| \leq p_{\max}$, and then k_s satisfies

$$
\frac{v_{\min}}{\varepsilon \sqrt{h^2 + p_{\max}^2}} \leq k_s \leq \frac{v_{\max}}{\varepsilon h}
\tag{53}
$$

where $v_{\min}$ and $v_{\max}$ is the minimum and maximum of v, respectively.

Integrating the both sides of Eq. (52) on the time interval $[0, +\infty]$ yields

$$
\int_0^{+\infty} \dot{V} \mathrm{d}t \leq -\int_0^{+\infty} (u_m - d_{2\max}) \|\boldsymbol{e}_{\tilde{R}}\|_1 + c k_s \|\boldsymbol{p}_{WP}\|_2^2 \, \mathrm{d}t
\tag{54}
$$

Hence,

$$
\int_0^{+\infty} (u_m - d_{2\max}) \|\boldsymbol{e}_{\tilde{R}}\|_1 + c k_s \|\boldsymbol{p}_{WP}\|_2^2 \, \mathrm{d}t \leq V(0) - V(\infty) \leq V(0)
\tag{55}
$$

Invoke Barbalat's lemma, we have

$$\lim_{t\to\infty} \boldsymbol{e}_{\tilde{R}} = \boldsymbol{0}, \ \lim_{t\to\infty} \boldsymbol{p}_{WP} = \boldsymbol{0} \tag{56}$$

Next, we will show that it is possible to prevent k from reaching 0 to avoid the singularity of the control scheme by choosing appropriate parameters. Considering the following equation

$$k\dot{k} = -\beta \left\{ u_m \alpha k^2 \left[\tanh\left(\frac{|e_1|}{\alpha k^2}\right) + \tanh\left(\frac{|e_2|}{\alpha k^2}\right) \right] + \boldsymbol{e}_{\tilde{R}}^{\mathsf{T}} \boldsymbol{\Pi}_R \tilde{\boldsymbol{R}}^{\mathsf{T}} \boldsymbol{\omega} \tanh\left(\frac{\boldsymbol{e}_{\tilde{R}}^{\mathsf{T}} \boldsymbol{\Pi}_R \tilde{\boldsymbol{R}}^{\mathsf{T}} \boldsymbol{\omega}}{\alpha k^2}\right) \right.$$

$$\left. + \alpha k^2 \tanh\left(\frac{|\boldsymbol{e}_{\tilde{R}}^{\mathsf{T}} \boldsymbol{\Pi}_R \tilde{\boldsymbol{R}}^{\mathsf{T}} \boldsymbol{\omega}|}{\alpha k^2}\right) + \left[\frac{cv}{\varepsilon}(\varepsilon+1) + cd_{1max}\right] \|\boldsymbol{p}_{WP}\|_2 \right\}$$

$$\geq -\beta \left\{ u_m(|e_1| + |e_2|) + 2\|\boldsymbol{e}_{\tilde{R}}\| \|\boldsymbol{\Pi}_R \tilde{\boldsymbol{R}}^{\mathsf{T}} \boldsymbol{\omega}\| + \left[\frac{cv}{\varepsilon}(\varepsilon+1) + cd_{1max}\right] \|\boldsymbol{p}_{WP}\|_2 \right\}$$

$$\geq -\beta \left\{ (u_m + 2\varDelta_\omega) \|\boldsymbol{e}_{\tilde{R}}\|_1 + \left[cv_{\max}\left(\frac{1}{\alpha-1}+1\right) + cd_{1max}\right] \|\boldsymbol{p}_{WP}\|_2 \right\} \tag{57}$$

where $\varDelta_\omega$ is the upper bound of ω. Integrating the both sides of Eq. (57) on the time interval $[0,+\infty]$ yields

$$\frac{1}{2}\left[k^2(+\infty) - k^2(0)\right] \geq -\beta \left\{ (u_m + 2\varDelta_p) \int_0^{+\infty} \|\boldsymbol{e}_{\tilde{R}}\|_1 \ \mathrm{d}t + c\left[v_{\max}\left(\frac{1}{\alpha-1}+1\right) + d_{1max}\right] \int_0^{+\infty} \|\boldsymbol{p}_{WP}\|_2 \ \mathrm{d}t \right\} \tag{58}$$

From Eq. (60), we known that

$$\int_0^{+\infty} \|\boldsymbol{e}_{\tilde{R}}\|_1 \ \mathrm{d}t \leq \frac{V(0)}{u_m - d_{2\max}} \tag{59}$$

$$\int_0^{+\infty} \|\boldsymbol{p}_{WP}\|_2^2 \ \mathrm{d}t \leq \frac{\varepsilon\sqrt{h^2 + p_{\max}^2}}{cv_{\min}} V(0) \tag{60}$$

According to the Cauchy-Schwarz inequality, one has

$$\left(\int_0^t \|\boldsymbol{p}_{WP}\|_2 \ \mathrm{d}t\right)^2 \leq \left(\int_0^t 1^2 \ \mathrm{d}t\right)\left(\int_0^t \|\boldsymbol{p}_{WP}\|_2^2 \ \mathrm{d}t\right) \tag{61}$$

That is

$$\frac{1}{t}\left(\int_0^t \|\boldsymbol{p}_{WP}\|_2 \ \mathrm{d}t\right)^2 \leq \int_0^t \|\boldsymbol{p}_{WP}\|_2^2 \ \mathrm{d}t \tag{62}$$

Evaluating the limits of the both sides of Eq. (62) yields

$$\lim_{t\to\infty} \frac{1}{t}\left(\int_0^t \|\boldsymbol{p}_{WP}\|_2 \ \mathrm{d}t\right)^2 \leq \frac{\varepsilon\sqrt{h^2 + p_{\max}^2}}{cv_{\min}} V(0) \tag{63}$$

Assume that $\lim_{t\to\infty}\left(\int_0^t \|\boldsymbol{p}_{WP}\|_2 \ \mathrm{d}t\right)$ is unbounded, and then the limit of the left part of Eq. (63) can be evaluated by

$$\lim_{t\to\infty} \frac{1}{t}\left(\int_0^t \|\boldsymbol{p}_{WP}\|_2 \ \mathrm{d}t\right)^2 = 2\lim_{t\to\infty} \|\boldsymbol{p}_{WP}\|_2 \left(\int_0^t \|\boldsymbol{p}_{WP}\|_2 \ \mathrm{d}t\right) \leq \frac{\varepsilon\sqrt{h^2 + p_{\max}^2}}{cv_{\min}} V(0) \tag{64}$$

Because $\|\boldsymbol{p}_{WP}\|_2 \leq p_{\max}$ and Eq. (64) holds independent of $\lim_{t\to\infty} \boldsymbol{p}_{WP} = \boldsymbol{0}$, it can be derived from Eq. (64) that $\lim_{t\to\infty}\left(\int_0^t \|\boldsymbol{p}_{WP}\|_2 \ \mathrm{d}t\right)$ is bounded, which conflicts with the assumption. Hence, one has

$$\lim_{t\to\infty}\left(\int_0^t \|\boldsymbol{p}_{WP}\|_2 \ \mathrm{d}t\right) \leq \wp \tag{65}$$

where $\wp > 0$ is a constant. According to Eq. (58), it is obvious that

$$k^2(+\infty) \geq k^2(0) - 2\beta V(0)\left\{\frac{u_m + 2\varDelta_p}{u_m - d_{2\max}} + \frac{c\wp}{V(0)}\left[v_{\max}\left(\frac{1}{\alpha-1}+1\right) + d_{1max}\right]\right\} \tag{66}$$

8

For a given $k(0) = k_0 > 0$, and a constant ϖ satisfying $0 < \varpi < k(0)$, there always exists a sufficiently small β satisfies

$$k_0^2 \geq \varpi^2 + 2\beta V(0) \left\{ \frac{u_m + 2\Delta_p}{u_m - d_{2\max}} + \frac{c\wp}{V(0)} \left[v_{\max} \left(\frac{1}{\alpha - 1} + 1 \right) + d_{1max} \right] \right\} \tag{67}$$

Thus,

$$k^2(+\infty) \geq \varpi^2 \tag{68}$$

In addition, recall that $k\dot{k} \leq 0$ and $k_0 > 0$, and therefore $k(t) \geq \varpi$, $\forall t > 0$. Evidently, the singularity of the proposed control scheme is avoided. ∎

4. Simulation Results

In this section, a 3D circle is taken as the desired path. The 3D circle presented by Eqs. (4)–(6) with $k_1(s) = 0.01$ and $k_2(s) = 0$. The velocity of the UAV is set to $v = 22\,\text{m/s}$, and the initial position of the UAV relative to $\mathcal{F}_P$ resolved in $\mathcal{F}_P$ is $\boldsymbol{p}_{WP}^P = [100, 10, 100]^\top$ m. The initial unit vector of the parallel frame resolved in $\mathcal{F}_I$ is

$$\boldsymbol{t}^I(0) = \left[\cos\left(\frac{\pi}{6}\right) \cos\left(\frac{\pi}{3}\right), \ \cos\left(\frac{\pi}{6}\right) \sin\left(\frac{\pi}{3}\right), \ \sin\left(\frac{\pi}{6}\right) \right]^\top, \tag{69}$$

$$\boldsymbol{n}_1^I(0) = \left[\sin\left(\frac{\pi}{3}\right), \ -\cos\left(\frac{\pi}{3}\right), \ 0 \right]^\top, \ \boldsymbol{n}_2^I(0) = \boldsymbol{t}^I(0) \times \boldsymbol{n}_1^I(0) \tag{70}$$

The initial rotation matrix from $\mathcal{F}_W$ to $\mathcal{F}_P$ is given by

$$\boldsymbol{R}_W^P(0) = \begin{bmatrix} 1 & 0 & 0 \\ 0 & 1 & 0 \\ 0 & 0 & 1 \end{bmatrix} \tag{71}$$

Fig. 2 gives the trajectories result from the path-following control schemes with an adaptive h or a constant h. In the initial phase, the UAV flies away from the desired path because the initial velocity vector points away from the path. After the initial adjustment, both the trajectories almost overlap the desired path finally, but the trajectory with the adaptive h approaches the desired path in a more preferable way. When the UAV is far from the desired path, the proposed path-following control scheme drives the UAV to move almost perpendicularly to the desired path. As the UAV is near the path, h becomes larger to make the velocity of the UAV tend to fly along the tangent of the path. The position of the UAV relative to the virtual target is illustrated in Fig. 3. It is seen that the position errors converge to the neighborhood of zero smoothly.
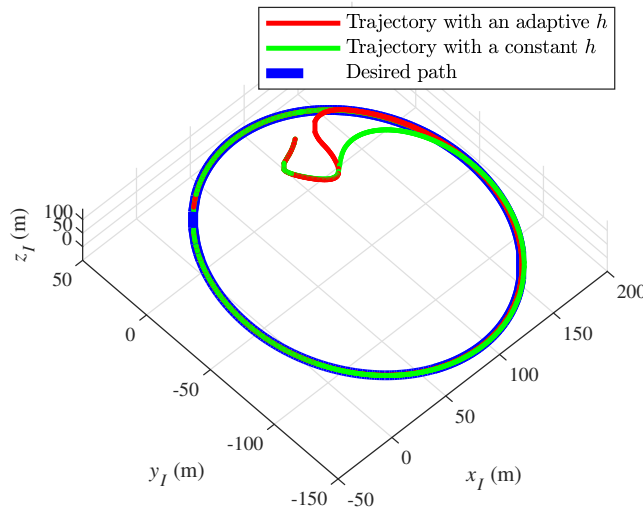

Figure 2 – Following trajectories with adaptive h or constant h.

Fig. 4 compares the convergence rate of the path-following control law with adaptive h to that with constant h. The result shows that the proposed control scheme converges more rapidly. The attitude errors between $\mathcal{F}_W$ and $\mathcal{F}_D$ are shown in Fig. 5, where the errors converge to zero accurately. In the profile of e_1, there is a hump above the zero line because control saturation occurs in this period. The saturation can be clearly seen in Fig.
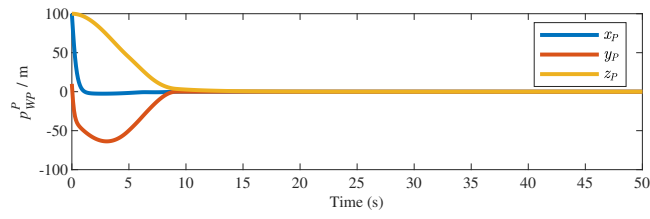
Figure 3 – Profiles of p_{WP}^P under the control of the proposed control scheme.
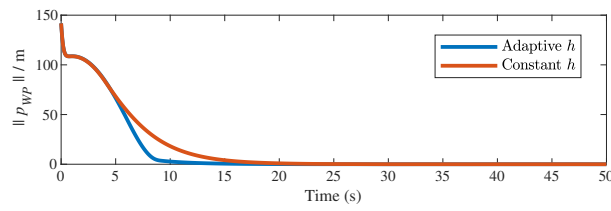
Figure 4 – Profiles of the distance between the UAV and the virtual target.
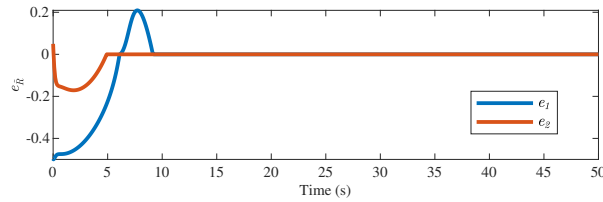

Figure 5 – Profiles of the attitude errors.
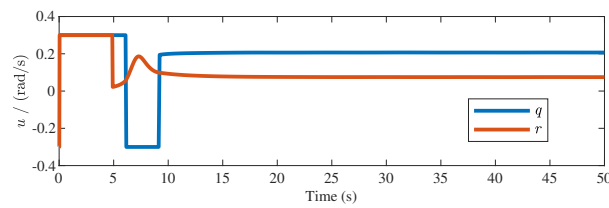
Figure 6 – Control input history of the proposed control scheme.

6. Though the angular velocity is restricted by physical limitations, the convergence of the path-following control is still guaranteed.

The velocity of the virtual target is plotted in Fig. 7. At the beginning of the path-following, the velocity of the virtual target is very large, but it does not saturate the control scheme because it is not a physical velocity. Evidently, the velocity of the virtual target converges to the velocity of the UAV finally. Fig. 8 gives the history of k. Though k decreases monotonically, it is lower bounded to avoid singularity as is proved previously.
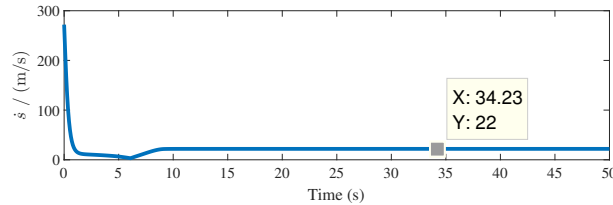
Figure 7 – History of $\dot{s}$.
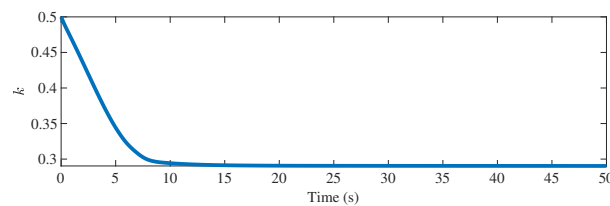
Figure 8 – History of k.

5. Conclusion

In this paper, an adaptive path-following control scheme is proposed for a fixed-wing UAV on SO(3) with input saturation and external disturbances considered. First, the path-following problem is formulated on SO(3) to derive the following errors. An auxiliary frame is constructed with an adaptive law for the parameter h introduced to make the path-following process converge fast and damp properly. Then, the control laws for the progression rate of the virtual target and the attitude of the UAV are proposed. The attitude control effort is bounded by using a hyperbolic tangent function with a variable gain. By virtue of the control laws, not only is the stability of the closed-loop system ensured but also the following performance is more preferable. The stability of the closed-loop system is proved via Lyapunov analysis and numerical simulations demonstrate the improvement on the path-following performance. In the future, the method in this paper can be extended to resolve the moving path-following problem.

6. Contact Author Email Address

The contact author email address is zhbo@nwpu.edu.cn.

7. Copyright Statement

8. Acknowledgements

References

[1] Rober N, Cichella V, Ezequiel Martin J, et al. Three-dimensional path-following control for an underwater vehicle. *J. Guid. Control Dyn.*, Vol. 7, No. 44, pp 1345-1355, 2021.

[2] Hu Q, Tan X, Akella M R. Finite-time fault-tolerant spacecraft attitude control with torque saturation. *J. Guid. Control Dyn.*, Vol. 10, No. 40, pp 2524-2537, 2017.

[3] Sujit P B, Saripalli S, Sousa J B. Unmanned aerial vehicle path-following: A survey and analysis of algorithms for fixed-wing unmanned aerial vehicles. *IEEE Control Systems*, Vol. 34, No. 1, pp 42-59, 2014.

[4] Rubí B, Pérez R, Morcego B. A survey of path-following control strategies for UAVs focused on quadrotors. *J. Intell. Robot. Syst.*, Vol. 98, No, 2, pp 241-265, 2020.

[5] Ollero A, and Heredia G. Stability analysis of mobile robot path tracking. *1995 IEEE/RSJ International Conference on Intelligent Robots and Systems/Human Robot Interaction and Cooperative Robots*, Piscataway, NJ, pp. 461-466, 1995.

[6] Sujit P B, Saripalli S, Sousa J B. An evaluation of UAV path-following algorithms. *2013 European Control Conference*, Zürich, Switzerland, pp. 3332-3337, 2013.

[7] Fossen T I, Breivik M, Skjetne R. Line-of-sight path-following of underactuated marine craft. *6th IFAC Conference on Manoeuvring and Control of Marine Craft*, Girona, Spain, pp. 211-216, 1997.

[8] Kothari M, Postlethwaite I, Gu D. A suboptimal path planning algorithm using rapidly-exploring random trees. *International Journal of Aerospace Innovations*, Vol 2, No. 1&2, pp. 93-103, 2010.

[9] Rokonuzzaman M, Mohajer N, Nahavandi S, et al. Review and performance evaluation of path tracking controllers of autonomous vehicles. *IET Intell. Transp. Syst.*, Vol. 15, No. 5, pp. 646-670, 2021.

[10] Wilhelm J P, Clem G. Vector field UAV guidance for path-following and obstacle avoidance with minimal deviation. *J. Guid. Control Dyn.*, Vol. 42, No. 8, pp. 1848-1856, 2019.

[11] Nelson D R, Barber D B, Mclain T W, et al. Vector field path-following for miniature air vehicles. *IEEE Trans. Robot.*, Vol. 23, No. 3, pp. 519-529, 2007.

[12] Pothen A A, Ratnoo A. Curvature-constrained Lyapunov vector field for standoff target tracking. *J. Guid. Control Dyn.*, Vol. 40, No. 10, pp. 2729-2736, 2017.

[13] Ali S U, Samar R, Shah M Z, et al. Higher-order sliding mode based lateral guidance for unmanned aerial vehicles. *Trans. Inst. Meas. Control*, Vol. 39, No. 5, pp. 715-727, 2017.

[14] Hamada Y, Tsukamoto T, Ishimoto S. Receding horizon guidance of a small unmanned aerial vehicle for planar reference path-following. Aerosp. Sci. Technol., Vol. 77, pp. 129-137, 2018.

[15] Chen Q, Wang X, Yang J, et al. Trajectory-following guidance based on a virtual target and an angle constraint. *Aerosp. Sci. Technol.*, Vol. 87, pp. 448-458, 2019.

[16] Jain R P, Sousa J B, Aguiar A P. Three dimensional moving path-following control for robotic vehicles with minimum positive forward speed. *IEEE Control Syst. Lett.*, Vol. 6, pp. 79-84, 2022.

[17] Cichella V, Kaminer I, Dobrokhodov V, et al. Geometric 3D path-following control for a fixed-wing UAV on SO(3). *AIAA Guidance, Navigation, and Control Conference*, Portland, Oregon, 2011.